

1.2 Test Case 2 Turbulent Water Transport in a Hydraulically Smooth Pipeline

1.2.1 Case Description

The test case considers turbulent water flow in a hydraulically smooth pipe. Owing to the inherent unsteadiness of turbulence, the flow is modeled in a time-averaged sense using the Reynolds-Averaged Navier-Stokes (RANS) equations coupled with eddy-viscosity turbulence models, within both wall-function and low-Reynolds frameworks. Exploiting axisymmetry, the mean flow is simulated as a 2D circular sector. A uniform axial velocity W_b with zero radial and azimuthal components and zero turbulence intensity is imposed at the inlet, zero external pressure at the outlet, and no-slip conditions at the walls.

1.2.2 Input Data

The input data for the simulation are provided in Table 3. The Reynolds number, calculated using Eq. 10, is greater than 2000, confirming that the flow is turbulent.

$$Re_b = \frac{W_b D}{\nu} = \frac{0.75 \times 0.1}{10^{-6}} = 75000 > 2000 \quad (10)$$

| Parameter | Value |
|---------------------------|----------------|
| Pipe Diameter D | $0.10m$ |
| Bulk Velocity W_b | $0.75m/s$ |
| Fluid Density ρ | $998.23Kg/m^3$ |
| Kinematic Viscosity ν | $10^{-6}m^2/s$ |
| Pipe Length L | $7m$ |

Table 3. Input Data

1.2.3 Entrance Length

The proposed equation for the entrance length in a circular pipe under turbulent flow conditions is given by Eq. 11. To verify that fully developed flow conditions are satisfied, the velocity profile is monitored at axial distances of 2.0, 3.0, 4.0, 5.0, and 6.0 m from the flow entrance, as shown in figure 14. It is evident that the velocity profile progressively develops into a parabolic shape along the axial direction. Beyond 4.0 m, the velocity profile shows negligible variation, indicating that the flow has reached a fully developed state. Moreover, the wall shear stress is monitored at the same locations and is observed to become nearly constant beyond 4.0 m, as shown in Figure 15.

$$L_e = (40 - 60)D = 4 \sim 6m \quad (11)$$

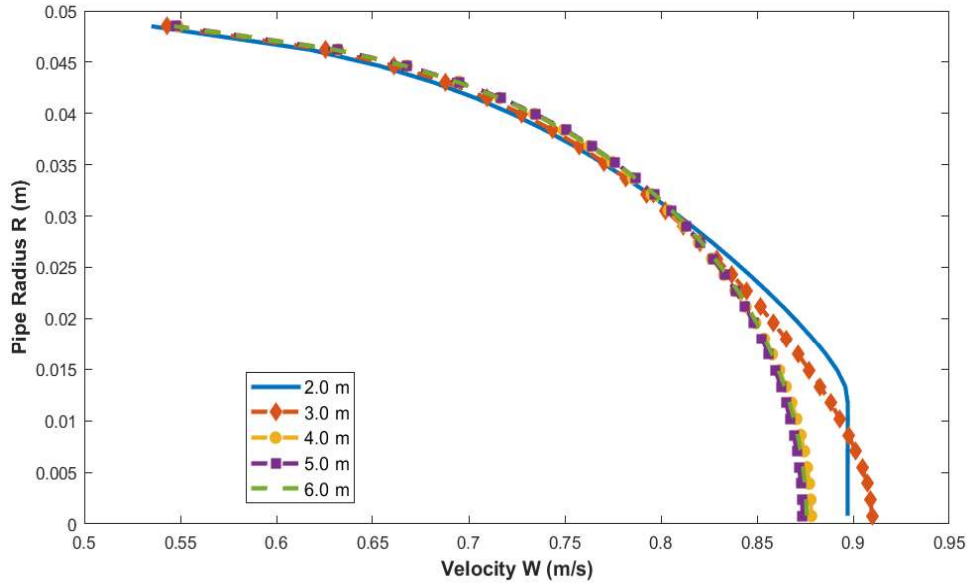


Fig. 14. Velocity (W) profile at 2.0, 3.0, 4.0, 5.0, and 6.0 m

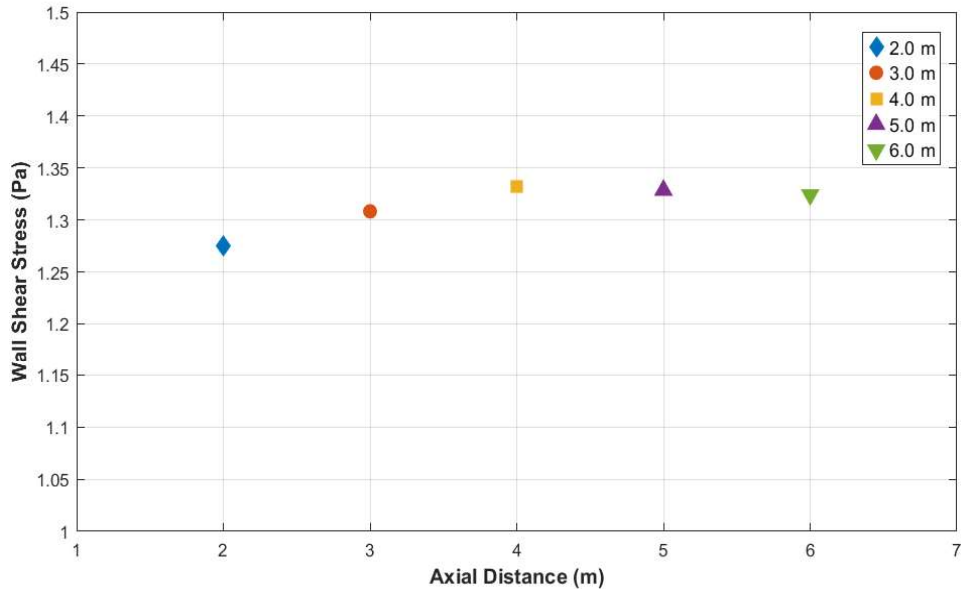


Fig. 15. Wall Shear Stress at 2.0, 3.0, 4.0, 5.0, and 6.0 m

1.2.4 Numerical Simulation

The simulation employs a mesh with 700 cells in the axial (Z) direction and 31 cells in the radial direction. The standard $k-\epsilon$ model is employed for turbulence, with the Launder–Spalding wall function. The first radial cell is sized to maintain a Y^+ value between 30 and 130 (Figure 16). Velocity and pressure contours along the pipe are presented in Figures 17 and 18. Downstream of the entrance length, the velocity profile develops into a parabolic shape, with the maximum velocity at the centerline. As the first cell center corresponds to $30 < Y^+ < 130$, the no-slip condition is not clearly visible in the velocity contours. The pressure decreases monotonically along the pipe, consistent with a pressure-driven flow.

1.2 Test Case 2 Turbulent Water Transport in a Hydraulically Smooth Pipeline

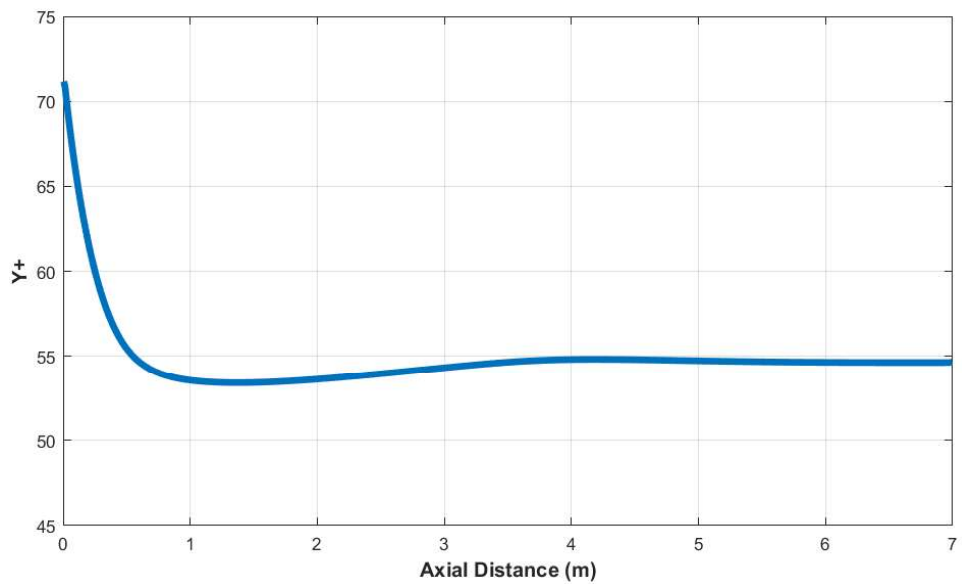


Fig. 16. Y^+ Value along the pipe

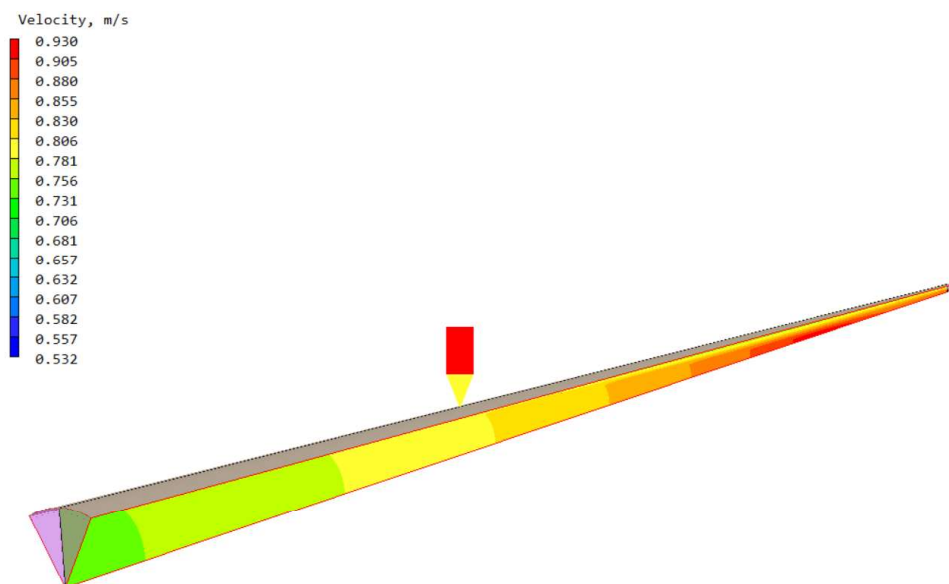


Fig. 17. Velocity Contours

1.2 Test Case 2 Turbulent Water Transport in a Hydraulically Smooth Pipeline

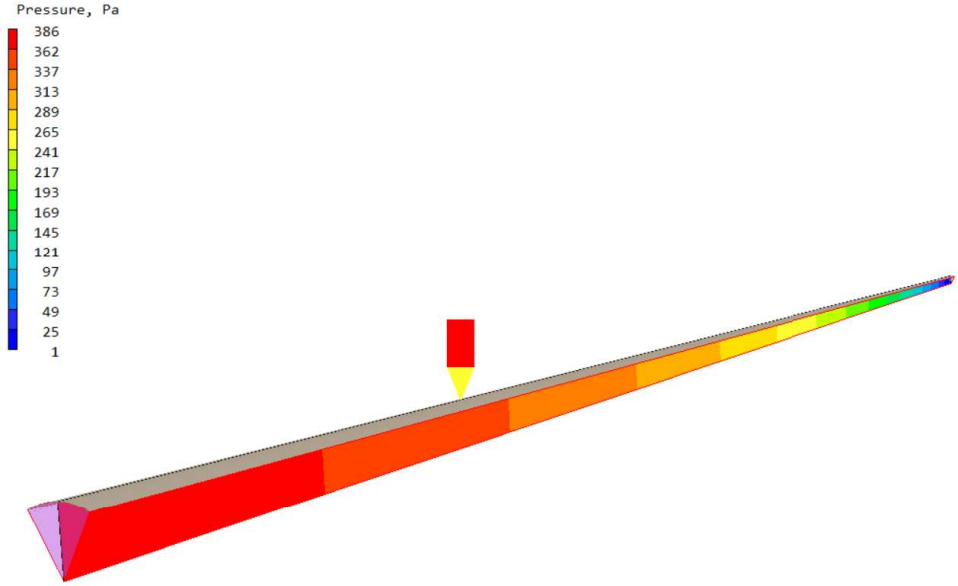


Fig. 18. Pressure Contours

The pressure distribution along the pipe and the friction factor are shown in Figure 19. The pressure distribution is linear, and the friction factor in the fully developed region is nearly $f = 0.0189$. The velocity profile at a distance of 6.0 m from the inlet is shown in Figure 20 in two dimensionless forms. The profile exhibits a parabolic shape, with a maximum at the centerline. The Reynolds stress, viscous shear stress, and total shear stress are shown in Figure 21. The viscous shear stress reaches its maximum near the wall; however, since the first cell center is located at $Y^+ > 30$, the wall shear stress cannot be directly resolved from the velocity gradients and is instead calculated using the wall function approach. The turbulent kinetic energy and dissipation rate are shown in Figure 22. The dissipation rate increases near the wall due to high velocity gradients, while both the kinetic energy and dissipation rate decrease near the centerline where the velocity gradients are small.

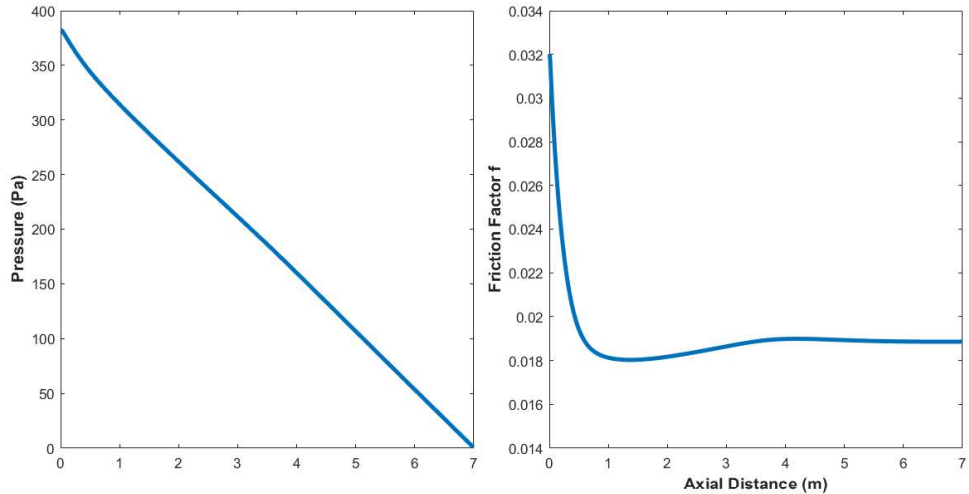


Fig. 19. Pressure Distribution (Left) and Friction Factor (Right)

1.2 Test Case 2 Turbulent Water Transport in a Hydraulically Smooth Pipeline

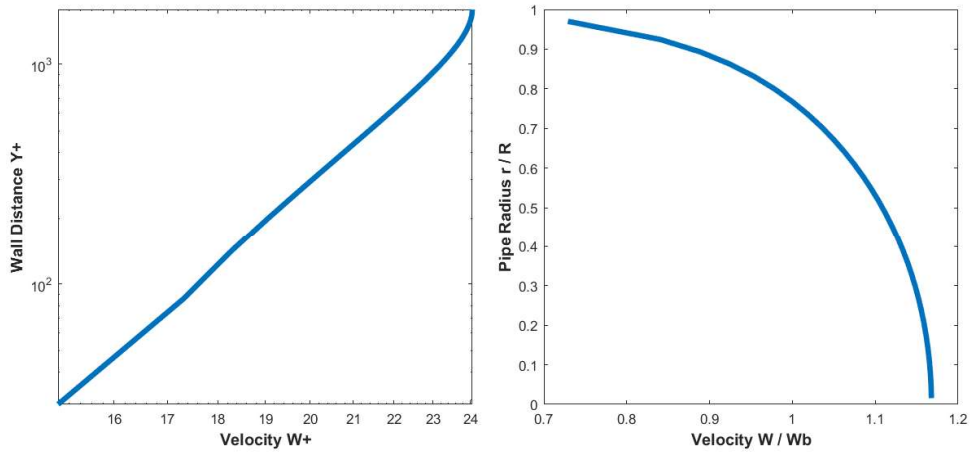


Fig. 20. Non-Dimensional Velocity Profiles

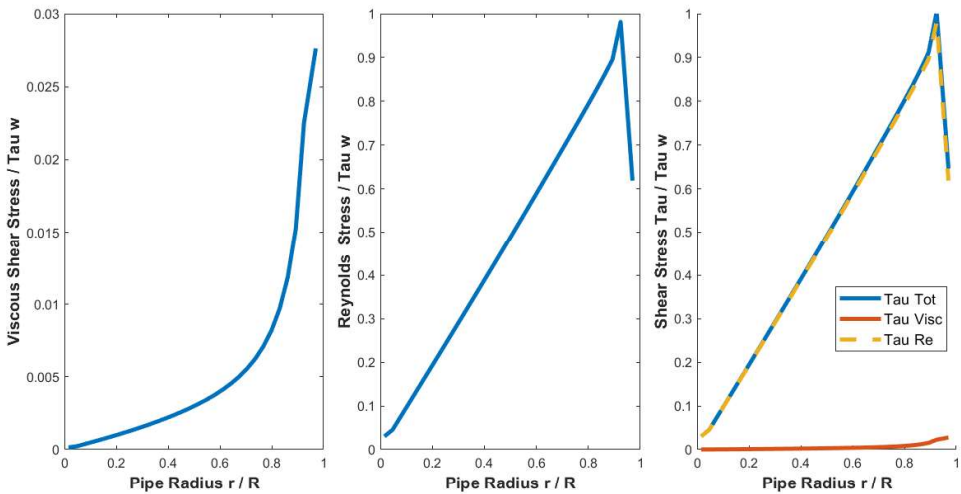


Fig. 21. Viscous Shear Stress (Left), Reynold's Stress (Middle), Total Shear Stress (Right)

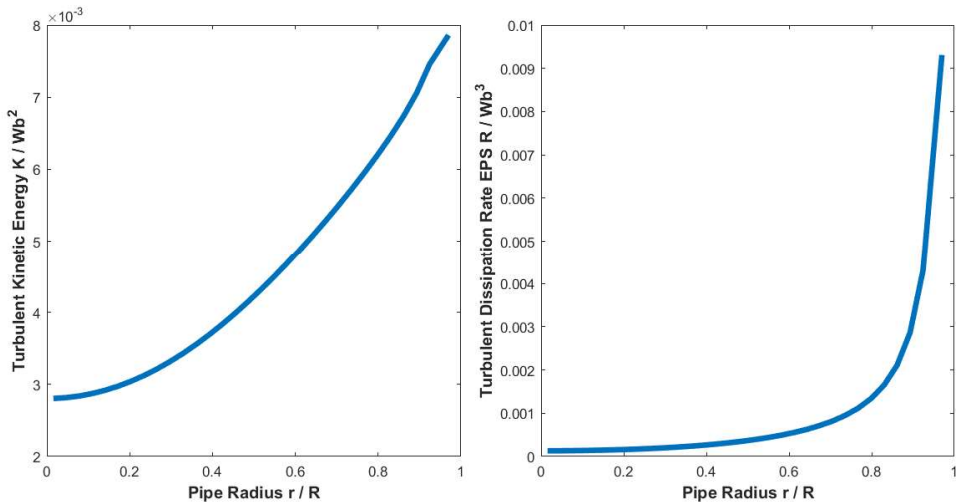


Fig. 22. Turbulent Kinetic Energy k (Left), Dissipation Rate ϵ (Right)

1.2.5 Numerical Convergence and Grid Independence

The normalized residuals of pressure, radial velocity, axial velocity, turbulent kinetic energy, and dissipation rate are monitored, and the solution is considered converged when all residuals fall below 1×10^{-3} , as shown in Figure 23.

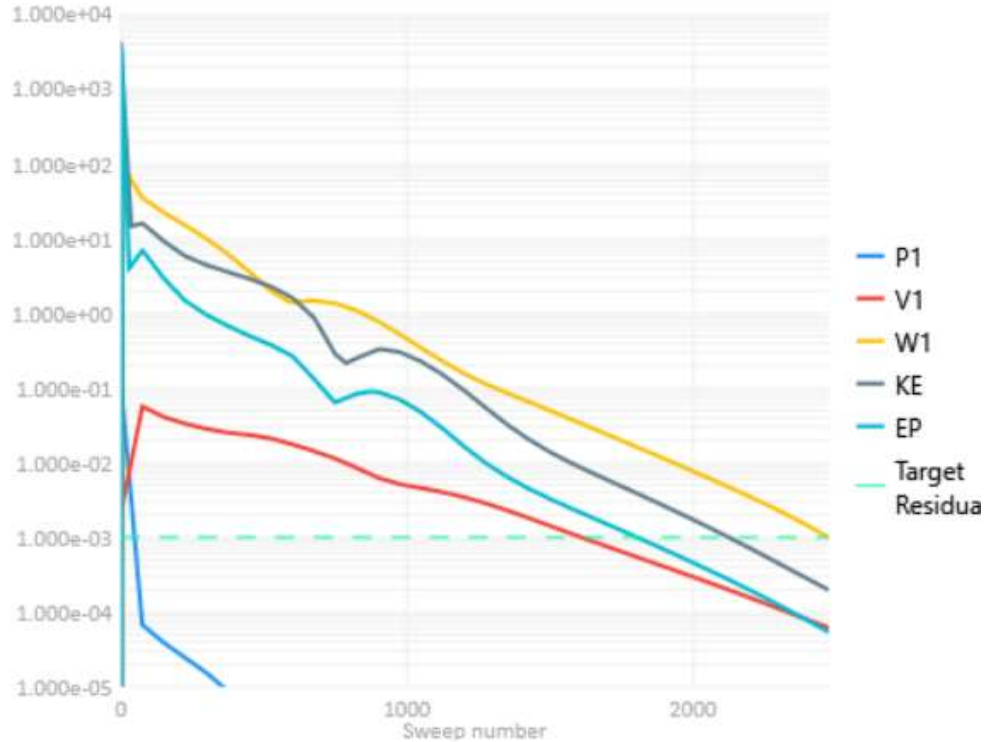


Fig. 23. Residuals

To assess grid independence, four meshes listed in Table 4 were considered. The wall shear stress, as well as the pressure and velocity at the pipe centerline at an axial location of 6.0 m from the inlet, were monitored (Figure 24). The variations are within acceptable limits for the three finest meshes. In addition, the velocity profile at 6.0 m from the inlet is shown in Figure 25, where the profiles obtained with different meshes overlap, confirming grid independence.

| Mesh | Elements in Radial Direction | Elements in axial Direction |
|--------------------|------------------------------|-----------------------------|
| Mesh 1 | 11 | 500 |
| Mesh 2 | 21 | 600 |
| Mesh 3 (Main Mesh) | 31 | 700 |
| Mesh 4 | 41 | 730 |

Table 4. Mesh Data

1.2 Test Case 2 Turbulent Water Transport in a Hydraulically Smooth Pipeline

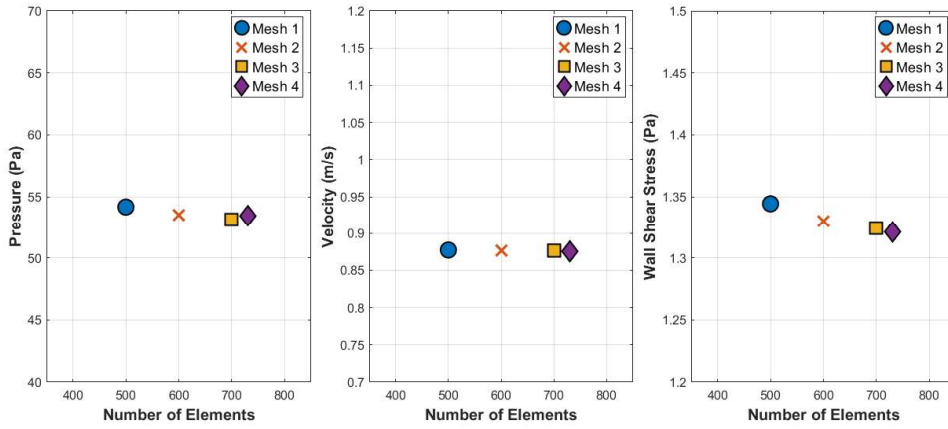


Fig. 24. Pressure, Velocity and Wall Shear Stress values at distance 6.0m from inlet for the 4 meshes

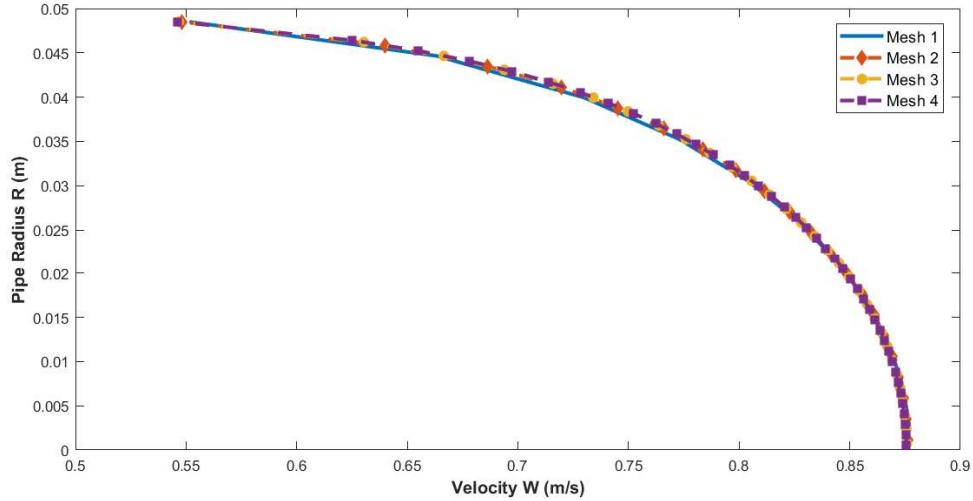


Fig. 25. Velocity profile at distance 6.0m from inlet for the 4 meshes

1.2.6 Validation

Experimental data from the PhD thesis of Lars Even Torbergsen (1998) are used for validation. Figure 26 presents the nondimensional velocity, turbulent kinetic energy, and dissipation rate. Although the CFD results do not exactly match the experimental data, they exhibit the same trends and are within acceptable limits.

1.2 Test Case 2 Turbulent Water Transport in a Hydraulically Smooth Pipeline

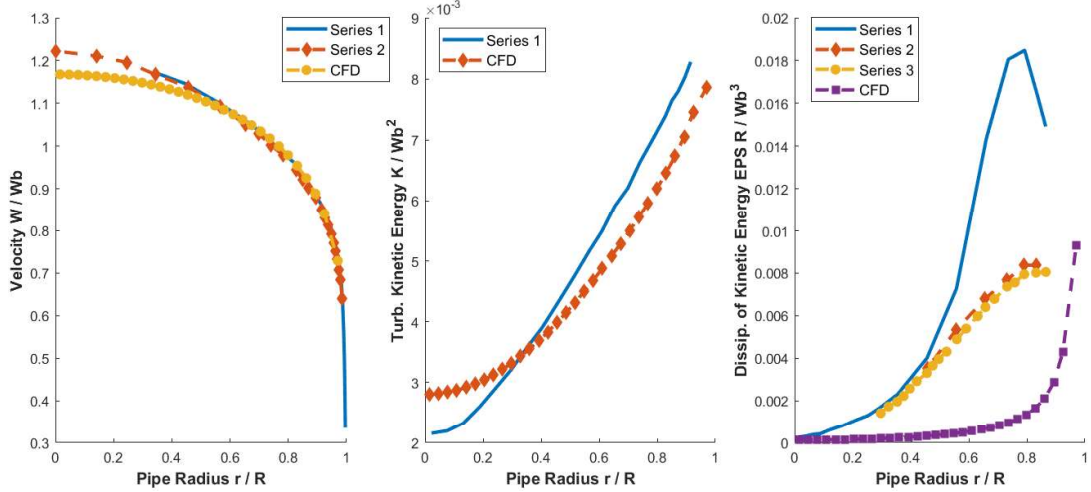


Fig. 26. Velocity, Turbulence Kinetic Energy and Dissipation rate

The friction factor obtained from the CFD simulation at 6.0 m from the inlet is $f = 0.0189$, as shown in Figure 19. For validation, the experimental value reported by Torberg sen is $f = 0.0191$. The friction factors predicted by the Prandtl and Haaland equations are 0.0191 and 0.0189, respectively, and the corresponding value from the Moody chart is shown in Figure 27. Overall, the CFD-predicted friction factor is consistent with the experimental data, empirical correlations, and the Moody chart.

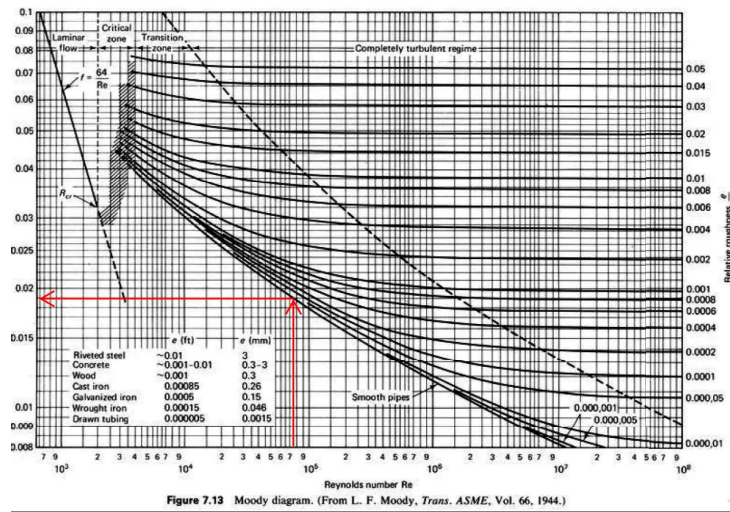


Fig. 27. Friction Factor extracted from Moody chart

Velocity validation is performed using the Nikuradse formula given by equation 12, where the exponent n is defined as $f^{-0.5}$. Three values of the friction factor are used to compute n : those obtained from the Prandtl formula, the Haaland formula, and the Moody chart. Figure 28 compares the CFD velocity profile with the Nikuradse prediction and the experimental data reported by Torberg sen.

$$\frac{W}{W_b} = \frac{(2n+1)(n+1)}{2n^2} (1 - r/R)^{1/n} \quad (12)$$

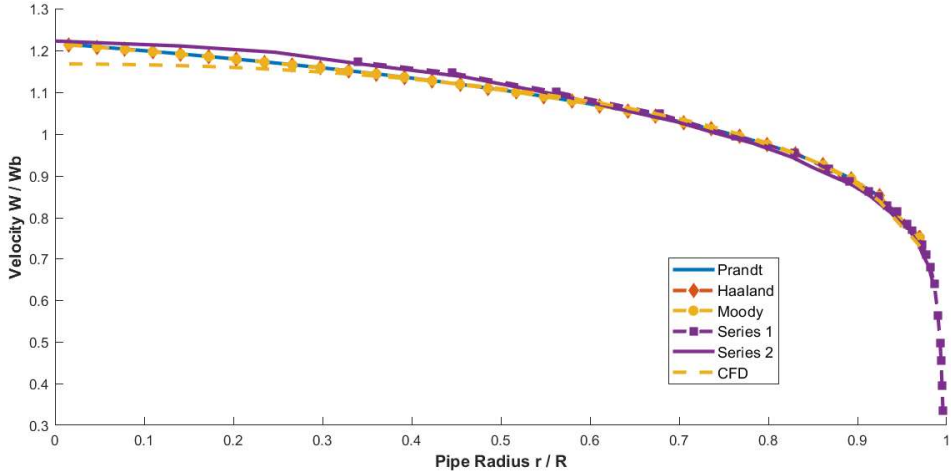


Fig. 28. Velocity validation using Nikuradse profile and results by Torbergesen

Another approach for velocity validation uses the Launder–Spalding formula given by Eq. 13. The results are compared with the CFD predictions, as shown in figure 29; however, since a wall-function approach is employed, the minimum Y^+ value is greater than 30. As a result, few data points fall within the valid range $11.6 < Y^+ < 130$, making this validation approach difficult to apply.

$$w^+ = \begin{cases} y^+ & y^+ < 11.6 \\ \frac{1}{k} \ln(Ey^+) & 11.6 < y^+ \leq 130 \end{cases} \quad (13)$$

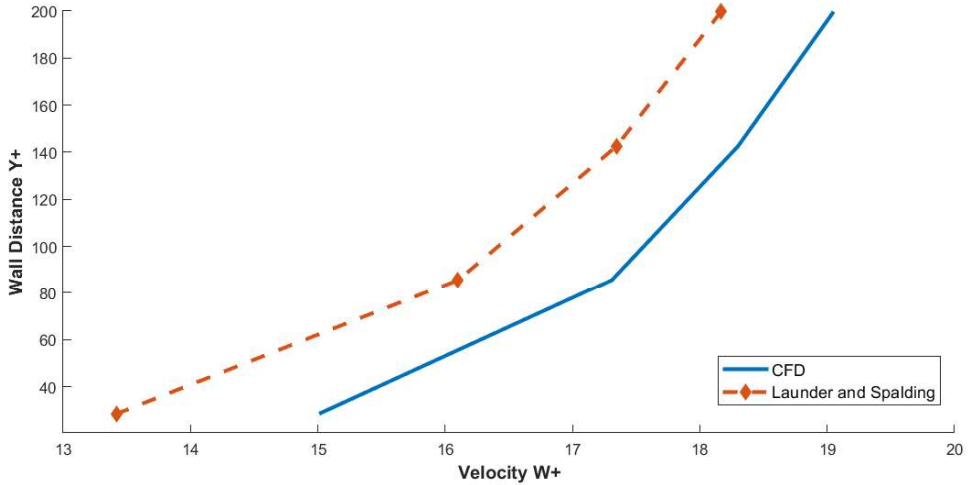


Fig. 29. Velocity validation using Launder and Spalding formula

The turbulent kinetic energy is validated against both the experimental data of Torbergesen and the empirical formula of Kam Hong Ng given by equation 14. As shown in Figure 30, the CFD-predicted turbulent kinetic energy agrees well with both the experimental data and the empirical formula, where the Kam Hong Ng results are evaluated using friction factors obtained from the Moody chart, Prandtl's formula, and the Haaland equation.

$$\frac{k}{W_b^2} = \frac{f}{8} \left[1 + \frac{2}{3} \left(\frac{r}{R} \right) + \frac{10}{3} \left(\frac{r}{R} \right)^3 \right] \quad (14)$$

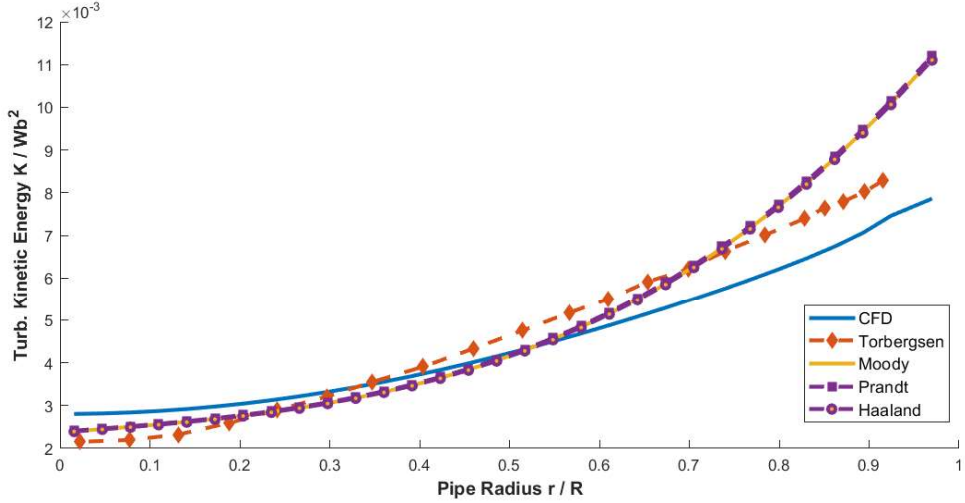


Fig. 30. Kinetic Energy Validation using Torbergsen data and empirical formula of Kam Hong Ng

The turbulent dissipation rate is validated against the experimental data of Torbergsen and the empirical formula given by Eq 15 and 16. As shown in Figure 31, the dissipation rate exhibits the same trend away from the wall, but accurate validation near the wall remains challenging.

$$\epsilon(r) = C_d \frac{k^{\frac{3}{2}}(r)}{l_m(r)} = 0.1643 \frac{k^{\frac{3}{2}}(r)}{l_m(r)} \quad (15)$$

$$l_m = R[0.14 - 0.08(\frac{r}{R})^2 - 0.06(\frac{r}{R})^4] \quad (16)$$

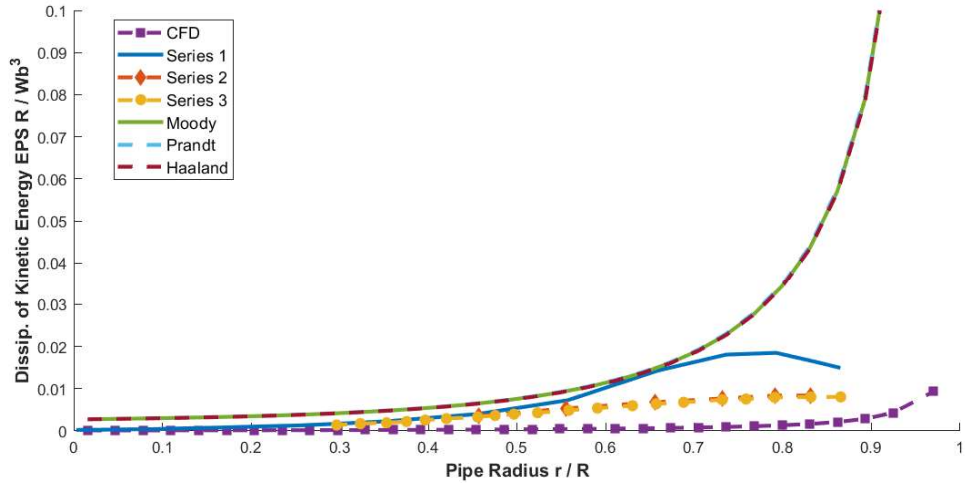


Fig. 31. Turbulent Dissipation Rate Validation

1.2.7 Influence of Turbulence Model

To assess the influence of the turbulence model, two additional variants of the standard $k - \epsilon$ model are considered: the RNG $k - \epsilon$ and the Realizable $k - \epsilon$ models, using the same wall-function approach. Figure 32 compares the results from the three turbulence models with the experimental data of Torbergsen. The CFD predictions are nearly identical for all three models

1.2 Test Case 2 Turbulent Water Transport in a Hydraulically Smooth Pipeline

and show good agreement with the experimental data. Moreover, the shear stress predicted by the three turbulence models is identical, as shown in Figure 33

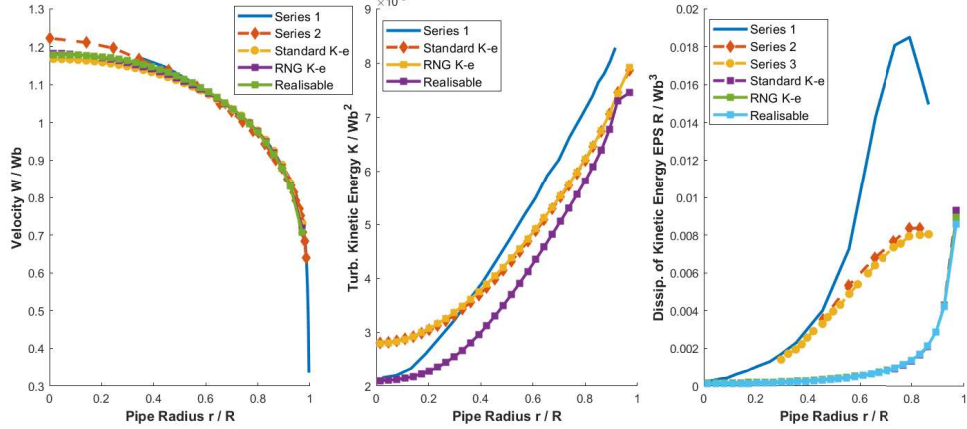


Fig. 32. Influence of Turbulence Models

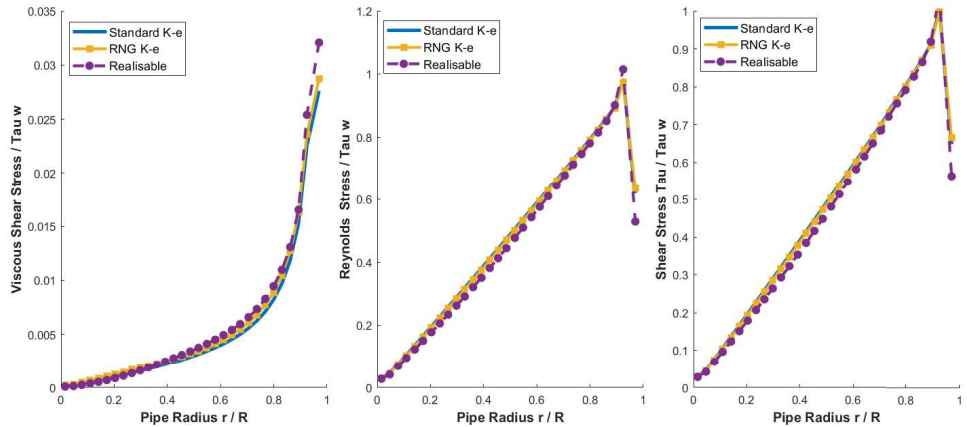


Fig. 33. Influence of Turbulence Models on Shear Stress

Another turbulence model considered is the two-layer $k - \epsilon$ model. Unlike the standard wall-function approach, this model employs a low-Reynolds-number formulation, resolving the near-wall flow field all the way to the viscous sublayer. Figure 34 compares the two-layer model, the standard $k - \epsilon$ model, and the experimental data. Regarding the velocity profile, both turbulence models show good agreement with the experimental results. However, differences become evident in the turbulent kinetic energy and dissipation rate distributions. The two-layer model extends the solution into the viscous sublayer and provides values for both turbulent kinetic energy and dissipation rate within this region. Specifically, the dissipation rate reaches a maximum inside the viscous sublayer before decreasing to zero at the wall. Similarly, the turbulent kinetic energy approaches zero at the wall, consistent with the physical boundary conditions.

1.2 Test Case 2 Turbulent Water Transport in a Hydraulically Smooth Pipeline

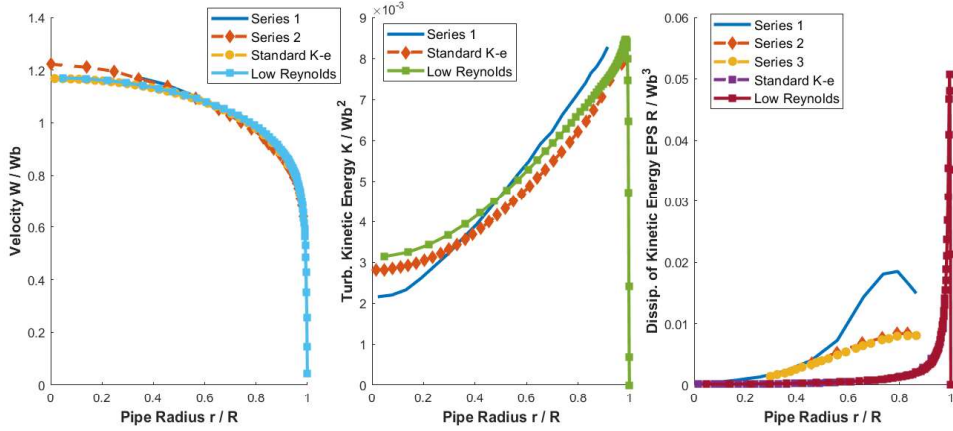


Fig. 34. Two Layer $k - \epsilon$ vs Standard $k - \epsilon$ vs Experimental Data

Since the two-layer model resolves the flow into the viscous sublayer, it can be observed, as shown in Figure 35, that the viscous shear stress dominates within this region, while the Reynolds shear stress approaches zero at the wall. In contrast, other turbulence models that employ the wall-function approach do not clearly capture this behavior, because the first computational cell is positioned within the logarithmic layer rather than the viscous sublayer.

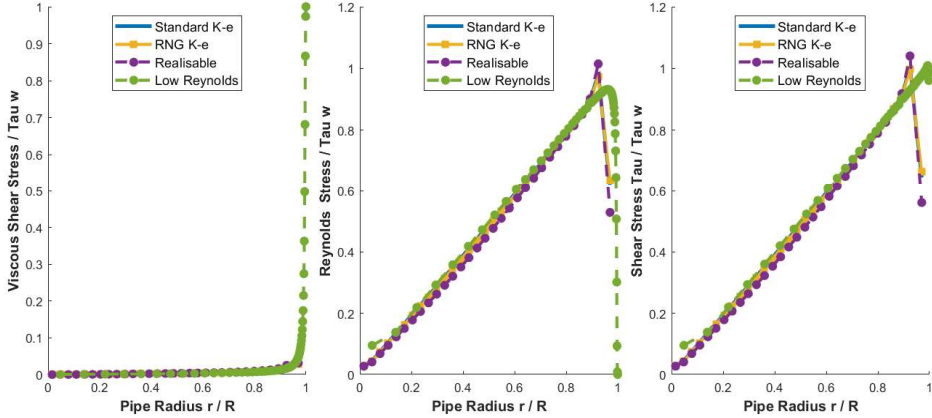


Fig. 35. Shear Stress for Different Turbulence Models